Microfluid Nanofluid
DOI 10.1007/s10404-007-0207-y

RESEARCH PAPER

Simulation-based analysis of flow due to traveling-plane-wave deformations on elastic thin-film actuators in micropumps

A. F. Tabak · S. Yesilyurt

Received: 21 November 2006 / Accepted: 28 March 2007

Abstract One of the propulsion mechanisms of microorganisms is based on propagation of bending deformations on an elastic tail. In principle, an elastic thin-film can be placed in a channel and actuated for pumping of the fluid by means of introducing a series of traveling-wave deformations on the film. Here, we present a simulation-based analysis of transient, two-dimensional Stokes flow induced by propagation of sinusoidal deformations on an elastic thin-film submerged in a fluid between parallel plates. Simulations are based on a numerical model that solves time-dependent Stokes equations on deforming finite-element mesh, which is due to the motion of the thin-film boundary and obtained by means of the arbitrary Lagrangian Eulerian method. Effects of the wavelength, frequency, amplitude and channel's height on the time-averaged flow rate and the rate-of-work done on the fluid by the thin-film are demonstrated and grouped together as the flow-rate and power parameters to manifest a combined parametric dependence.

1 Introduction

The potential for low-cost mass-production of microfluidic components such as micropumps has appeal for medical, environmental, biotechnology, electronic packaging, space exploration and energy applications where micropumps can be used and dispensed, for example, for drug delivery, sensor measurements, on-chip experiments, DNA replication, micro-propulsion, microelectronic cooling, and fuel delivery (Polla et al. 2000; Meyns et al. 2000; Gardeniers and van den Berg 2004; Wang and Lee 2005; Bruschi et al. 2002; Zhang et al. 2002; Zhang and Wang 2006). Especially for liquids, overwhelming dominance of viscous forces compared to inertial forces in micro scales limits the implementation of transduction mechanisms in micropumps, which can be, in general, magnetic, electric or mechanical (Laser and Santiago 2004). Electrically conducting and magnetic fluids can be forced to flow by means of a magnetic field (Lemoff et al. 1999; Jang and Lee 2000; Homsy et al. 2005). However, the presence of electric currents may not suitable for many applications (Homsy et al. 2005). The charge distribution due to polarization of the solid–liquid interface, as well as due to free ions in the fluid results in a net controllable, steady, electro-osmotic flow when the electric field is applied externally (Dutta and Beskok 2001; Polson and Hayes 2000).

Mechanical reciprocating positive-displacement pumps are more common than dynamic pumps as the latter cannot perform adequately for highly viscous fluids, or at very low Reynolds numbers of the microscopic world. Reciprocating pumps consist of a diaphragm membrane or a piston, and at least one or two check valves or nozzle-diffuser type components to move and direct the flow (Van Lintel et al. 1988; Zengerle 1995). High flow rates are obtained only with the application of large voltages to piezoelectric-material drivers (Li et al. 2000; Feng and Kim 2005). A few drawbacks of these mechanical pumps include complexity of the design, and unsteady flow rates (Bourouina et al. 1997). Producing controllable steady flows with mechanical micropumps remains somewhat a challenge.

Propulsion mechanisms of microorganisms can be a viable option in producing controllable flows with

A. F. Tabak · S. Yesilyurt (✉)
Faculty of Engineering and Natural Sciences,
Sabanci University, Istanbul, Turkey
e-mail: syesilyurt@sabanciuniv.edu

micropumps. Microorganisms such as spermatozoa and bacteria use their flagella to propel themselves (Brennen and Winet 1977; Purcell 1977). Bacterial flagella, which create a screw-like motion, are usually helically shaped and driven by a rotary engine at the base. Flagella of spermatozoa and other eukaryotic cells resemble to elastic rods, whose stress-induced sudden-bending deformations propagate towards the tip in a way similar to beating motion (Gray and Hancock 1955). Periodic traveling-wave deformations of the biopolymer tail of the microorganism are the result of optimal balance between the structural bending and viscous forces that lead to the propulsion of the organism (Lowe 2003). In principle, the mechanism that enables the propulsion of these microorganisms can be used as a pump when an elastic thin-film, on which the deformation waves are formed and propagated, is placed in a channel.

Sir Taylor presented an analysis of the flow that takes place when an infinite inextensible sheet is immersed in viscous fluid and propagated sinusoidal waves of small constant amplitude (Sir Taylor 1951). In addition to Taylor's analysis of inextensible sheets, there is a body of work on the hydrodynamics analysis of the low Reynolds number flow due to propagation of waves on a slender body (hair-like structures), which is summarized by Brennen and Winet (1977).

Here, we aim to demonstrate and analyze the mechanism of shear-induced pumping due to large deformations traveling as sinusoidal waves on an elastic thin-film immersed in a fluid by means of parametric transient simulations of the flow. Since the moving boundary is completely immersed in the fluid, the net volumetric change is zero, and the flow is merely due to dynamic effects, namely, shear interactions as in the case of propulsion of microorganisms (Gray and Hancock 1955). In particular, vertical motion of the elastic film brings about high and low pressure regions in the fluid and a flow between them. As the deformations shift position, say in the y-direction, according to the propagation of traveling waves in the x-direction, so does the high and low pressure spots, which, in turn, lead to a net flow in the same direction as the waves propagate.

We assume that it is plausible to manufacture an elastic thin-film and an actuation mechanism that will yield useful traveling-wave deformations. For example, piezoelectric components with large shear modes sandwiched between structural components are capable of causing large bending deformations, which can be manipulated to travel on the structure (Piefort 2001; Piefort and Henrioulle 2000). Alternatively, electrostatic actuators, which are designed for extended displacement such as described in Zhang and Dunn (2002), are very promising as they also operate at low voltages.

The unsteady flow over the thin-film that constitutes moving boundaries between parallel plates has very low Reynolds number, and, hence, is modeled using two-dimensional time-dependent Stokes equations. The fluid–structure interaction due to moving boundary is modeled with the arbitrary Lagrangian Eulerian (ALE) method incorporating the Winslow smoothing (Duarte et al. 2004). Using commercial software, COMSOL (COMSOL AB 2007), we carried out a number of simulations to find out and describe the parametric dependence of the flow rate and the rate-of-work done on the fluid by the film with respect to amplitude, wavelength and frequency of the waves, and the channel's height. In this analysis, we focused on the maximum mean flow rate and the power exerted on the fluid, detailed simulations with respect to varying pressure loads and efficiency calculations are presented elsewhere (Tabak and Yesilyurt 2007). Moreover, our emphasis is on the analysis of the flow enabled by the motion of the actuator boundary, rather than the structural analysis of the deformation of the thin film and the design of the mechanism for the actuation of this motion, which are discussed in part by (Tabak 2007).

2 Methodology

Consider an elastic-thin film, which is immersed in a fluid halfway between parallel plates of separation H as shown in Fig. 1. The film moves only in the y-direction vertically according to traveling plane-wave bending deformations that propagate in the x-direction and are described by traveling sine-waves

$$y_{\mathrm{f}}\left(x_{\mathrm{f}},t\right) = B(x_{\mathrm{f}},t)\sin\left(\omega t - kx_{\mathrm{f}}\right), \tag{1}$$

where y_{f} is the time and position-dependent vertical displacement of the film, $B(x_f,t)$ is the amplitude of the wave that depends on the local x-position, x_{f}, which is measured from the tip on the film, and time t, $\omega = 2\pi f$ is the angular frequency, f is the frequency, and $k = 2\pi/\lambda$ is the wave-number of plane-wave deformations. The thickness of the film is neglected compared to its length and width, which is in the z-direction and not shown in Fig. 1. Our analysis is based on a generic shape and propagation of deformations on the thin-film regardless of structural manipulations required to obtain this type of traveling displacements. In fact, the time and position dependent amplitude, B in (1), may vary based on the limits of the actual thin-film structure and its actuation mechanism.

Flow induced by the motion of boundaries according to (1) is governed by Stokes equations, which neglect the inertial term in the Navier–Stokes equations as the viscous forces dominate and the incompressible flow in the channel has a very low Reynolds number. Namely, we have

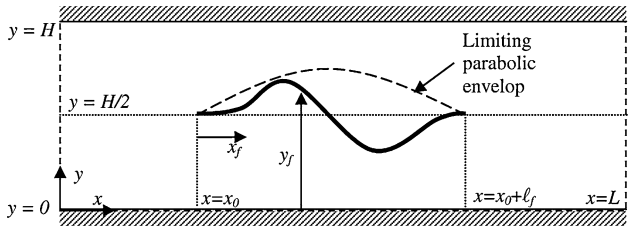

Fig. 1 Wave propagation on a elastic thin film placed in a microchannel filled with an incompressible fluid

$$\rho\left(\frac{\partial \mathbf{U}}{\partial t} - \mathbf{u}_{\text{mesh}} \cdot \nabla \mathbf{U}\right) = -\nabla p + \mu \nabla^2 \mathbf{U} \quad \text{in} \quad \Omega(t), \tag{2}$$

and

$$\nabla \cdot \mathbf{U} = 0 \quad \text{in} \quad \Omega(t), \tag{3}$$

In (2), $\mathbf{U} = [u,v]'$ is the velocity vector, which comprises of its x and y components, i.e. u and v, p is the pressure, ρ is fluid's density, μ is the dynamic viscosity of the fluid, and $\Omega(t)$ is the volume occupied by the fluid at time t. The domain, $\Omega(t)$, is defined with fixed boundaries, which correspond to the channel's walls, inlet and outlet, and moving boundaries that coincides with the film's surface. The $\mathbf{u}_{\text{mesh}} = [u_{\text{mesh}}, v_{\text{mesh}}]$ in (2) represents the deformation velocity of the time-varying domain $\Omega(t)$ and its coordinates with respect to the initial fixed frame, $\Omega(0)$, i.e. $u_{\text{mesh}} = \partial x/\partial t$, and $v_{\text{mesh}} = \partial y/\partial t$, where x and y are the coordinates in $\Omega(t)$ (Duarte et al. 2004; COMSOL AB 2007).

Boundary conditions for the Stokes equation are no-slip conditions on the plate walls,

$$\begin{bmatrix} u(x,0,t) \\ v(x,0,t) \end{bmatrix} = \begin{bmatrix} u(x,H,t) \\ v(x,H,t) \end{bmatrix} = \begin{bmatrix} 0 \\ 0 \end{bmatrix}; \tag{4}$$

velocity on moving boundaries of the actuator film is zero in the x-direction, and equal to the time-derivative of the vertical deformation given by (1) for the vertical component

$$u(x_f, y_f, t) = 0, \quad v(x_f, y_f, t) = \frac{dy_f}{dt} = \left(\frac{dB(x,t)}{dt}\right)\sin(\omega t - kx_f) + \omega B(x,t)\cos(\omega t - kx_f) \tag{5}$$

In (5), x_f and y_f represent the time-dependent position of the thin-film with respect to the reference frame. Note that, although partial derivatives of y_f and B with respect to x_f are non-zero, since x_f does not change with time, vertical component of the film velocity can be calculated from (5).

At the channel inlet and outlet, unless otherwise noted, we use the neutral flow boundary conditions (COMSOL AB 2007), which correspond to vanishing total forces acting on the surface

$$[-p\mathbf{I} + \boldsymbol{\tau}] \cdot \mathbf{n}|_{x=\{0,L\},y,t} = \mathbf{0}, \tag{6}$$

where $\mathbf{n}$ is the outward normal of the surface, and $\boldsymbol{\tau}$ is the viscous stress tensor (Landau and Lifshitz 2005).

Note that we can specify the total pressure force on inlet and outlet boundaries alternatively, however solution may not always converge as the pressure constraint becomes too stringent on the flow for all wavelengths, amplitudes, and frequencies. Therefore, we relaxed that condition in our general parametric study, with neutral boundary conditions that the flow is not restricted at the inlet and the outlet of the micropump.

Initial condition for (2) is the flow at rest, i.e. the velocity components and the pressure are all equal to zero at $t = 0$:

$$u(x,y,0) = v(x,y,0) = p(x,y,0) = 0. \tag{7}$$

Stokes equations (2), which are subject to incompressibility (3), boundary (4–6), and initial conditions (7) are discretized using triangular Lagrange elements that use quadratic basis functions for the velocity and linear ones for pressure.

Apparent velocity of the mesh $\mathbf{u}_{\text{mesh}}$ in (2), needs to be calculated due to the propagation of the motion of the boundary into the fluid domain. The ALE method that incorporates Winslow smoothing (Duarte et al. 2004; COMSOL AB 2007; Winslow 1967) is used to obtain the velocity of the deforming mesh on which the Stokes equations are solved. The mesh velocity $\mathbf{u}_{\text{mesh}}$, is calculated from the solution of the Laplace equation in the reference frame, which allows smooth deformation of internal nodes according to the deformation of boundary nodes (Duarte et al. 2004):

$$\nabla^2 \mathbf{u}_{\text{mesh}} = 0 \quad \text{in} \quad \Omega(t), \tag{8}$$

Alternatively, one can prescribe an appropriate distribution of internal nodes as long as it leads to a smooth distribution of the nodal points inside $\Omega(t)$ without solving (8) (COMSOL AB 2007). In two-dimensional calculations, solution of (8) is not costly, however in three-dimensional calculations adoption of the latter strategy may prove more practical (Tabak 2007).

The boundary conditions, which (8) is subject to, are moving boundary conditions on the thin-film, akin to (5), and the zero mesh-displacement elsewhere. Namely,

$$\begin{aligned} u_{\text{mesh}}(x_f, y_f, t) &= 0, \\ v_{\text{mesh}}(x_f, y_f, t) &= \frac{dy_f}{dt} = \left(\frac{dB(x,t)}{dt}\right)\sin(\omega t - kx_f) \\ &+ \omega B(x,t)\cos(\omega t - kx_f), \end{aligned} \tag{9}$$

and

$$\begin{bmatrix} u_{\text{mesh}}(0,y,t) \\ v_{\text{mesh}}(0,y,t) \end{bmatrix} = \begin{bmatrix} u_{\text{mesh}}(L,y,t) \\ v_{\text{mesh}}(L,y,t) \end{bmatrix} = \begin{bmatrix} u_{\text{mesh}}(x,0,t) \\ v_{\text{mesh}}(x,0,t) \end{bmatrix} = \begin{bmatrix} u_{\text{mesh}}(x,H,t) \\ v_{\text{mesh}}(x,H,t) \end{bmatrix} = \begin{bmatrix} 0 \\ 0 \end{bmatrix} \tag{10}$$

Having calculated the mesh velocity $\mathbf{u}_{\text{mesh}}$, from (8), one can find the updated mesh in $\Omega(t)$ and solve Stokes equations given by (2). The Laplace equation in (8) is solved using the same triangulation of the domain as the one used for the solution of the Stokes equations. Quadratic basis functions are used for the mesh velocity components as well in the finite-element procedure (COMSOL AB 2007).

Time and position-dependent amplitude of the traveling-wave deformations on the thin film is specified by a simple parabola that reaches to its full shape during the first period, and thereafter remains steady

$$B(x_{\text{f}},t) = 4B_0(1 - x_{\text{f}}/\ell_{\text{f}})(x_{\text{f}}/\ell_{\text{f}}) \min(t, 1/f), \tag{11}$$

where f is the frequency of the oscillations ℓ_f is the length and, and B_0 is the maximum deformation of the thin-film. Time-averaged quantities are calculated for periods in which a steady-periodic state is achieved after the initial ramp.

The instantaneous flow rate per unit depth delivered by the pump for a given set of inputs $\{B_0, f, \lambda, H\}$, is computed by the integration of the x-component of the velocity over the inlet or outlet of the channel as given by

$$Q(t) = Q_{\{\text{in,out}\}}(t) = \int_{y=-H}^{H} \mathbf{u}(t) \cdot (\mp \mathbf{n}_{\{\text{in,out}\}}) \text{d}y, \tag{12}$$

where $\mathbf{n}_{\text{in}}$ and $\mathbf{n}_{\text{out}}$ correspond to inlet and outlet surface normals (outward), due to which the '+' sign applies for the outlet flow, and '–' for the inlet flow. In practice, we also check the conservation of mass by comparing inlet and outlet flow rates, the relative difference of which always remains well below the tolerance of the numerical procedure, i.e. $2|Q_{\text{in}} - Q_{\text{out}}|/|Q_{\text{in}} + Q_{\text{out}}| \approx 10^{-8} < 10^{-3}$.

The time-averaged flow rate is computed from the integral of instantaneous flow rate given by (12) over at least three full periods of plane-wave deformations after a steady-periodic state is observed

$$\bar{Q} = \bar{Q}_{\{\text{in,out}\}} = \frac{1}{(k-i)/f} \int_{t_i=i/f}^{t_k=k/f} Q_{\{\text{in,out}\}}(t) \text{d}t, \quad i,k \in \mathbb{N},\ i<k-2 \tag{13}$$

Due to relatively short length of the channel and the dominance of viscous effects the flow becomes steady-periodic within the first period following the initial ramp of plane-wave deformations.

The rate of work done on the fluid by the deforming motion of the film is calculated by the area integral of the product of the film's y-velocity and the y-component of the total stress tensor on the film

$$\Pi(t) = \int_{\text{Film surface}} \Sigma_{\text{y}}(x_{\text{f}},y_{\text{f}},t) v(x_{\text{f}},y_{\text{f}},t) dA \tag{14}$$

where Π is the rate of work (power) done on the fluid (also called "shaft power" in classical texts such as in Munson et al. 2006), Σ_{y} is the y-component of the stress tensor, which is exerted by the structure on the fluid, and v is the y-velocity of the film given by (5). Total y-stress on the fluid is given by Batchelor (2000)

$$\Sigma_{\text{y}}(x_{\text{f}},y_{\text{f}},t) = \left(2\mu\frac{\partial v}{\partial y} - p\right)n_y + \mu\left(\frac{\partial u}{\partial y} + \frac{\partial v}{\partial x}\right)n_x, \tag{15}$$

where, μ is the viscosity of the fluid, n_x and n_y are x- and y-component of the surface normals. The time-averaged power is calculated the same way as the time-averaged flow rate, which is calculated by (13).

3 Results

Our numerical results are presented in terms of dimensionless quantities, which are scaled with appropriate characteristic scales of length, time and velocity and fluid properties; the base case is as shown in Table 1. Unless otherwise noted, these scales are used in the simulations. Moreover, default values of dimensionless geometric variables are listed in Table 2; where the superscript '*' denotes nondimensional quantities.

The film actuator is defined as an ellipsoid with the small axis being 5×10^{-3} units, and the large one 5 units. This small thickness is introduced to distinguish between the upper and lower normals of the film.

Table 1 Characteristic scales and their base values used in simulations and comparison of results

Characteristic scales	Representative values
Length (ℓ_0)	2.5×10^{-4} m
Velocity (U_0)	5×10^{-4} m/s
Time (t_0)	0.5 s
Pressure and shear (p_0)	ρU_0^2, 2.5×10^{-4} Pa for water
Power (Π)	$\rho \ell_0^2 U_0^3$, 7.81×10^{-15} W for water

Table 2 Default values for geometric variables used in simulations, unless otherwise noted

Geometric variables (dimensionless)	Value
Channel height (H^*)	2.5
Channel length (L^*)	9.0
Film's length, ℓ_f^*	5.0
Maximum amplitude of the deformation for general case (B_0^*)	0.0581
Wavelength (λ^*)	5.0
Frequency (f^*)	1.0
Wave speed (c^*)	5.0

3.1 Flow regimes

In Fig. 2, a series of snapshots of the pressure and velocity distribution in the channel is shown for $f^* = 1.0$, $\lambda^* = \ell_f^* = 5$ and $B_0^* = 0.365$. First half of the full period between $t^* = 3.9$ and 4.9 is covered in the snapshots. The other half of the period is mirror-symmetric with respect to the channel centerline. At a given instant, such as any snapshot shown in Fig. 2a–e, higher pressure takes place on the side of the film that pushes the fluid than the side which pulls the fluid. In other words, a particular point on the film is exposed to a higher pressure above the film than below when the slope of the film at that point is negative and lower pressure than the one below when the slope is positive as the waves travel in the x-direction. These high and low pressure couples move downstream at the same velocity as the speed of wave propagation. Once the high (low) pressure point on the film passes the midpoint, it starts decreasing its intensity; and reaches to its lowest when the film takes the shape of a 'Mexican hat' (see Fig. 2c), which corresponds to the largest deformation of the midpoint. As the wave travels further downstream and the slope of the film changes, high and low pressure regions switch sides; high pressure takes place under and low pressure above the film. Note that Fig. 2d ($t^* = 4.3$) is the mirror image of 2b ($t^* = 4.0$) and 2e ($t^* = 4.4$) of 2a ($t^* = 3.9$).

Furthermore, in combination with the local vertical motion of the film, net pressure difference across the film introduces a moment and accompanied recirculation in the fluid. As the recirculation moves downstream it results in a net flow rate in the channel albeit smaller than the local flow rate takes place above or below the film. The relative size of the velocity arrows indicates the local speed in Fig. 2a–e.

At any given instant and x-position on the film x_f, the sum of the two flows on both sides of the film must be equal to the total flow rate

$$Q(t) = Q_{\text{top}}(x_f, t) + Q_{\text{down}}(x_f, t), \tag{16}$$

where

$$Q_{\text{top}}(x_f, t) = \int_{y_f}^{H} u(x_0 + x_f, t)\mathrm{d}y, \tag{17}$$

and

$$Q_{\text{down}}(x_f, t) = \int_{0}^{y_f} u(x_0 + x_f, t)\mathrm{d}y. \tag{18}$$

Hence, for the flow rate to be positive at all times, either both Q_{up} and Q_{down} must be positive at any position on the film, or when one is negative the other must be positive and have a larger magnitude. In Fig. 3, total flow rate and relative variations of Q_{top}^* and Q_{down}^* for $x_f = \ell_f/2$ are shown with respect to time. The net flow rate $Q^*(t)$, remains always positive, but oscillates between its minimum, 0.77, and maximum values, 0.99. The partial flow rate above and below the film, are also steady-periodic but oscillates between -1.25 and 2.02 for the case shown in Fig. 3. When the flow rate above the film reaches its maximum, the flow rate below the film becomes the minimum and vice versa.

The y-profile of the x-component of the velocity at the midpoint of the channel is shown for $t^* = 4.15$, 4.3, 4.35, 4.4, 4.45, 4.5, and 4.65 in Fig. 4. The y-position of the film at the midpoint, $y_f(\ell_f/2, t)$, is maximum when $t^* = 4.15$ and minimum when $t^* = 4.65$. At $t^* = 4.15$, the x-component of the velocity is in the negative direction above the film, and in the positive direction below confirming what is observed in Fig. 3. At $t^* = 4.3$, the flow passing the midpoint slows down in magnitude both above and below the film; this corresponds to diminishing intensity of the high and low pressures. At $t^* = 4.35$, flow above the film changes its direction near the film; net flow rate above the film at that time is about zero (see Fig. 3). At $t^* = 4.40$, deformation of the film at the midpoint is zero and the x-velocity profiles above and below the film are almost identical and positive corresponding to $Q_{\text{top}}^* = Q_{\text{down}}^* = 0.494$ (Fig. 3). At $t^* = 4.45$, velocity profile above (below) the film is similar to the velocity profile below (above) the film at $t^* = 4.35$. This is also valid for $t^* = 4.50$ and 4.30, and $t^* = 4.65$ and 4.15. From that time forward, the evolution of the velocity profile is reversed until $t^* = 5.15$, when the cycle is completed.

Figure 5a, b depict the pressure distribution and Fig. 5c shows the u-velocity and streamlines in the channel for the case which corresponds to small wavelengths compared to the length of the film. Namely, we have $\lambda^*/\ell_f^* = 1/11, f^* = 1$, and $B_0^* = 0.058$. In this simulation,

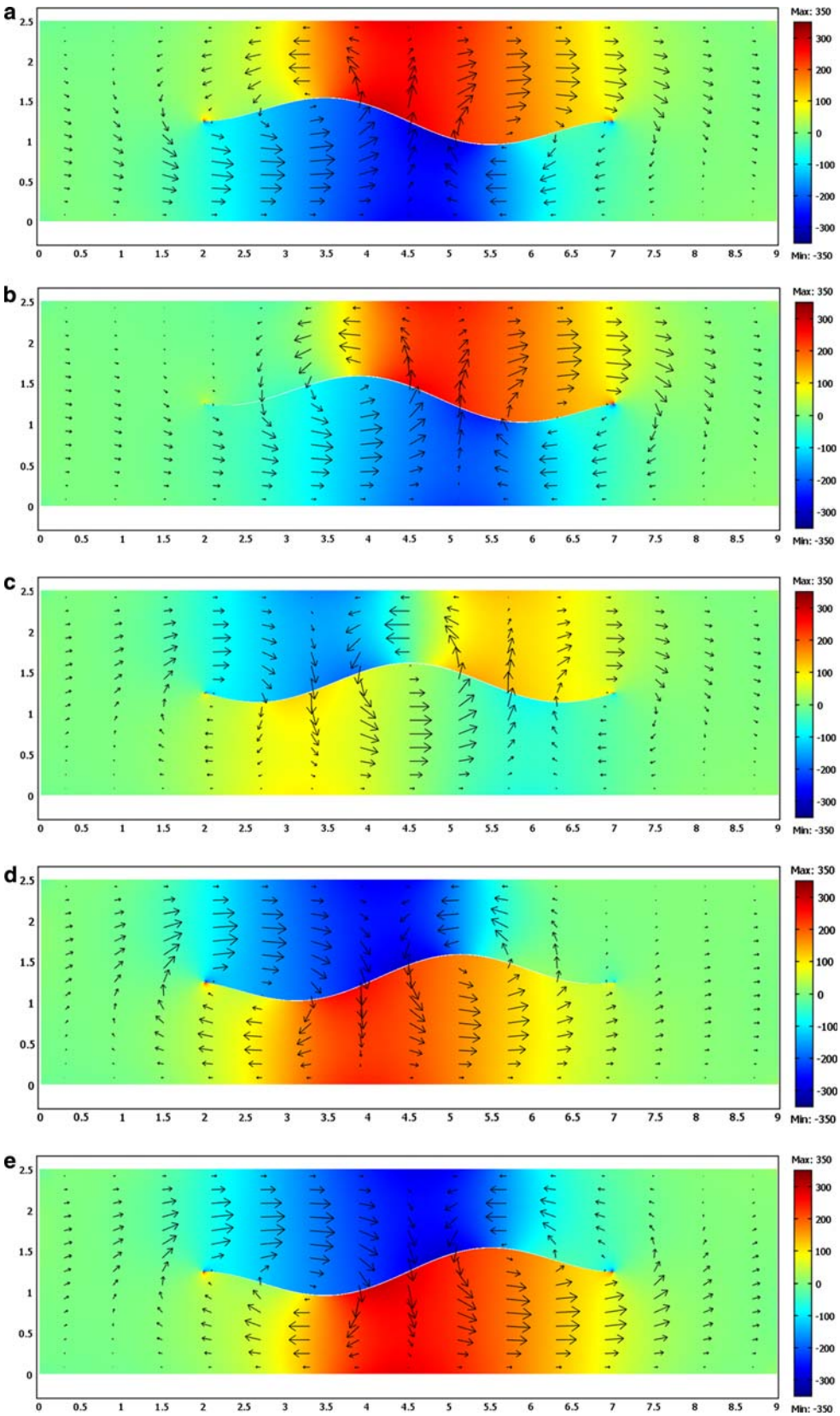

Fig. 2 H*=2.5, B0* = 0.365, $\lambda^* = \ell f^* = 5$,f* = 1; snapshots of the pressure distribution (*color shading*), and flow velocity (*arrows*) for t* = 3.9,4.0,4.15,4.3, and 4.4, respectively from **a** to **e**. The length of the arrows is proportional to local magnitude of the velocity

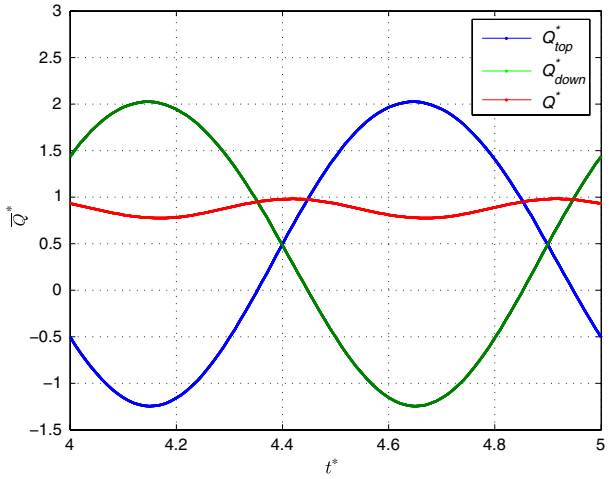

Fig. 3 Flow rates through top and down side of the elastic film and the net flow

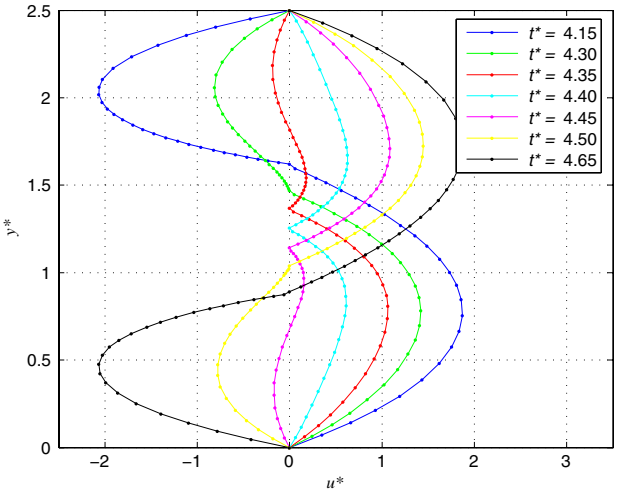

Fig. 4 The y-profile of the x-component of the velocity on the midpoint of the film

the length scale is kept the same as in Table 1, and the time scale is, t_s = 5.5 s. According to Fig. 5a, high and low pressure regions are distributed in the close vicinity of the film on both sides. Similarly to what is shown in Fig. 2a–e, pressure is higher when the slope of the surface is positive and lower when negative above the film. However there are multiple pairs of high and low pressure regions on both sides of the film corresponding to a multitude of waves on the film as shown in Fig. 5a. Maximum and minimum pressures are closer to deformation peaks. We omitted multiple snapshots, as the pressure changes locally near the film only. In fact, in Fig. 5b, the pressure distribution along the channel is shown at y^* = 2.0 and t^* = 4.0 (along the line in Fig. 5a)—note that, this profile remains almost steady and does not change significantly in time.

The pressure profile in Fig. 5b is typical for a dynamic pump placed in a channel, where the pressure first drops due to friction in the channel prior to the position where pumping takes place, increases due to pumping action, and, finally, decreases again due to friction in the exit portion. Corresponding u-velocity distribution and streamlines are shown in Fig. 5c, which does not vary significantly in time near the walls confirming a steady flow in that region and varies with respect to traveling waves near the film. Inlet and exit portions of the channel correspond to almost steady-laminar parabolic profiles as indicated by color shading of the u-velocity. Moreover, there is a steady circulation pair in the middle of the channel on both sides of the film near the walls indicating that average u-velocity must be higher near the film. In essence, instantaneous streamlines indicate that the time-averaged velocity distribution is similar to that of converging-diverging nozzles.

A special case of the flow regime takes place when the amplitude of the waves is comparable to the height of the channel. In the limit, when $B_0 = H/2$ the pump in fact works as a displacement pump, where the deformation waves on the film carries the fluid steadily.

Another flow regime is a trivial case when the wavelength is much larger than the length of the film. In this case, the net flow rate goes to zero and the effectiveness of the pump diminishes. The film simply deforms according to (1) with a parabolic deformation profile not yielding a significant net flow.

3.2 Parametric dependence of flow rate and power

In what follows, characteristic scales that are presented in Table 1 are used to obtain dimensionless quantities.

Figure 6a depicts the relationship between the channel-height-to-amplitude ratio, H/B_0, and the time and area-averaged velocity, $\bar{U}^* = \bar{Q}^*/H^*$, which decreases with the square of the H/B_0 ratio. This behavior is consistent with what is reported by Katz (1974) in the analysis of the propulsion of an infinitely extending sheet placed between parallel plates and subject to traveling deformation-waves. Katz observed that velocity normalized with the speed of wave propagation is proportional to the square of B_0/H ratio when $H/\lambda \sim O(1)$ according to,

$$\frac{\bar{U}_\infty}{c} = \frac{C_1}{(H/B_0)^2 + C_2}, \tag{19}$$

where C_1 and C_2 are positive constants, and $\bar{U}_\infty$ is the time-averaged velocity of the infinite sheet. Relationship given by (19) is predominant regardless whether the amplitude or the channel height is varied in simulations. Moreover, in Fig. 6a, it is shown that the average velocity converges to the displacement-pump limit, which is characterized by the amplitude of the waves being equal to the

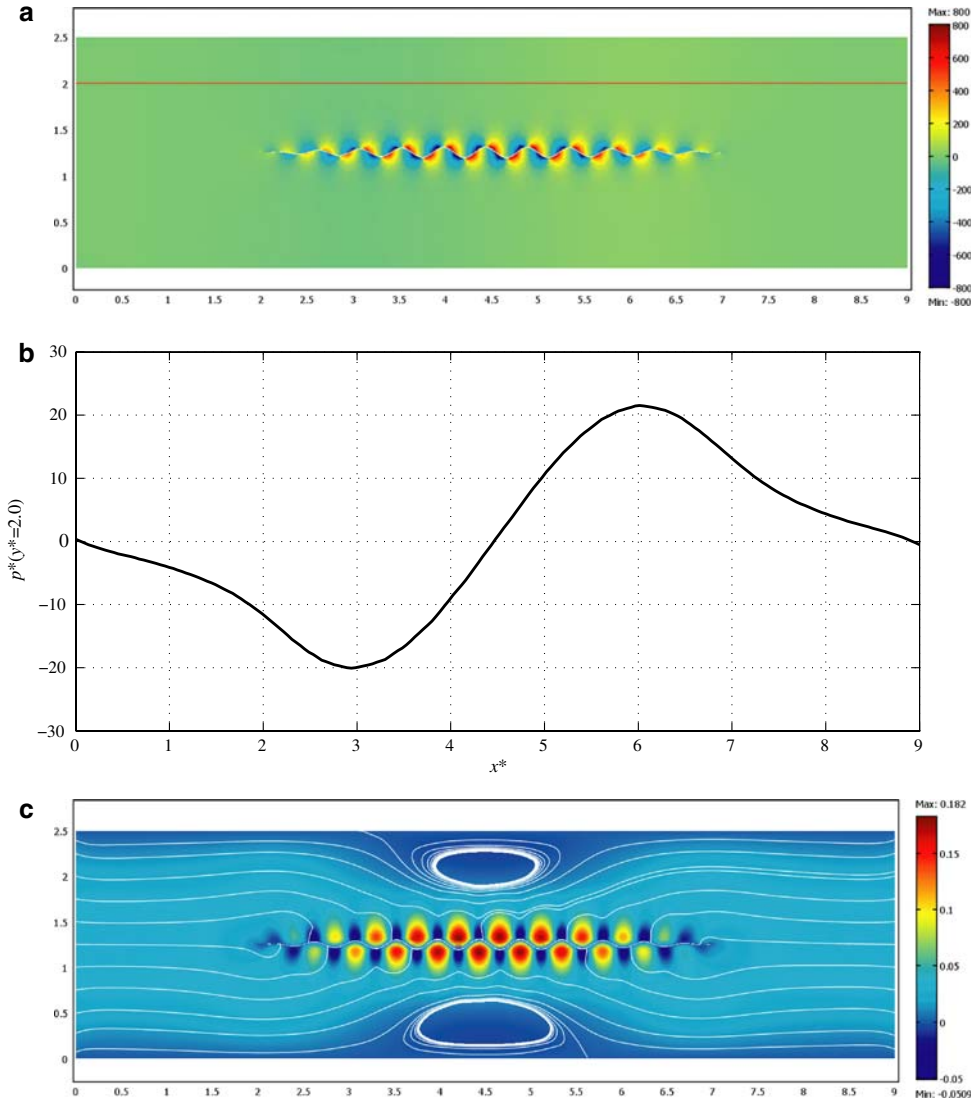

Fig. 5 For $\lambda/\ell_f = 11, f^* = 1, B_0^* = 0.058$ at $t^* = 4.0$: **a** color shaded pressure distribution; **b** pressure plot along the line in **a**; **c** color shaded u-velocity distribution and streamlines

half of the channel's height. In that case, essentially, the average velocity of the flow is the same as the propagation speed of the waves.

In Fig. 6b, time-averaged nondimensional rate of work done on the fluid by the elastic film is calculated from (14,15) based on dimensionless quantities, and plotted against the H/B_0 ratio. Rate of work decreases with the square of H/B_0 especially in the case for variable amplitude runs. In effect, this result agrees qualitatively well with the asymptotic analysis presented by (Childress 1981) for the time-averaged work per unit horizontal area per time for the infinite sheet, which results in quadratic dependence of power on the amplitude:

$$\bar{\Pi}_\infty = C_\Pi 2\mu \frac{\omega^2 B_0^2}{\lambda} \tag{20}$$

where the proportionality constant, C_Π is equal to one for the infinite sheet. Furthermore, variable height runs deviate from the square dependence due to the relative change in other variables such as λ, which has a profound effect on the flow regime as discussed in Sect. 3.1 and shown in Figs. 2a–e and 3a–c.

In Fig. 7a, the relationship between the time-averaged flow rate and the frequency of the deformation waves is shown. It is clear that the average flow rate tends to increase linearly with the frequency. This is also observed by Sir Taylor in the analysis of swimming microorganisms, which is modeled as having a sheet of infinite extension that propagates deformation waves in the opposite direction to the swimming direction in an infinite medium without walls (Sir Taylor 1951). In Taylor's analysis the average velocity of the microswimmer has a leading term proportional to the frequency of deformations on the film

$$\bar{U}_{s,\infty} \approx k^2 B^2 c \sim \frac{B^2 \omega}{\lambda} \tag{21}$$

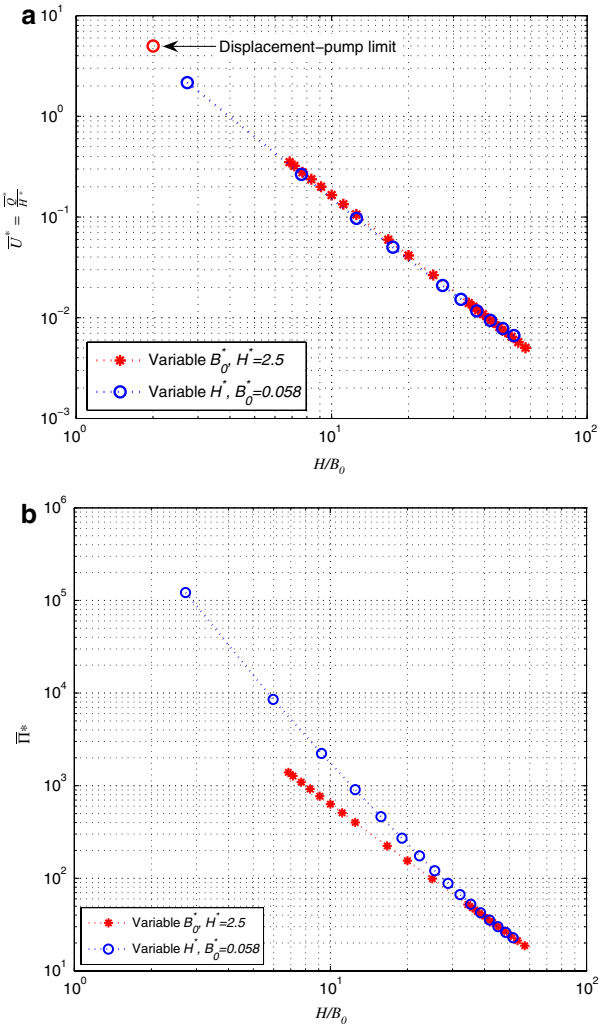

Fig. 6 **a** Parametric dependence of the time and area averaged velocity with respect to channel-height to wave amplitude ratio, H/B_0, displacement-pump limit is indicated for $H/B_0 = 2$ and $\bar{U}^* = c^* = 5$; **b** parametric dependence of the time-averaged power exerted on the fluid by the film with respect to H/B_0 for varying H and B_0

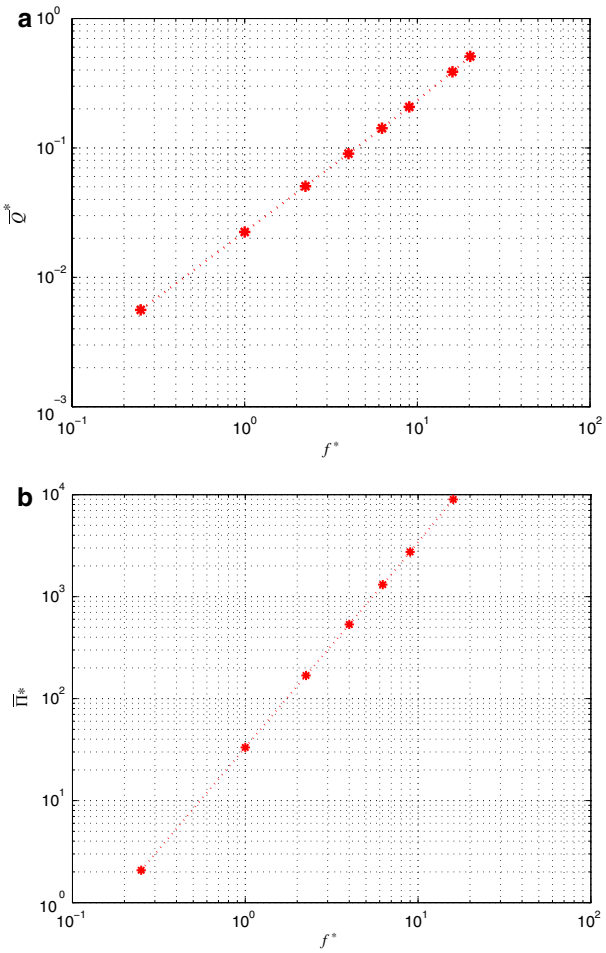

Fig. 7 **a** Time-averaged flow rate as a function of the frequency of the sinusoidal deformations on the film; **b** Time-averaged dimensionless power exerted on the fluid as a function of the frequency

Based on (19) and (21), it is plausible to expect the average velocity, hence the flow rate for constant channel height, constant amplitude and constant wavelength to have a linear dependence on the frequency.

Figure 7b demonstrates the behavior of time-averaged nondimensional power exerted on the fluid, which is calculated from (14), with respect to driving frequency. Power exerted by elastic thin film tends to increase with the square of frequency, which qualitatively agrees well with the result of the analysis presented in (Childress 1981) and given by (20).

In Fig. 8a, average flow rate is plotted against the wavelength. As reported in Figs. 2 and 3, the wavelength, in fact, determines the flow regime that takes place in the channel. For small wavelengths, almost-steady flow rate in the channel decreases slowly with the wavelength agreeing well with the Taylor's result given in (21). As the wavelength becomes comparable with the separation of channels, which is half of the length of the film, steady-periodic flow rate increases proportional to the square root of the wavelength rather than the linear dependence suggested by (19). Note that the analysis, which is the basis of the result presented in (19), is for an infinitely long sheet unlike the finite film considered here and for which $\lambda/H \approx O(1)$. It is presumable to suggest that the deviation is due to film's finite-length, and further studies are necessary to elucidate this behavior. Moreover, due to the finite length of the film further increase of the wavelength is expected to reduce the flow rate as the envelope given in (11) reduces the effectiveness of the wave propagation.

In Fig. 8b, time-averaged power calculated by (14) is plotted as a function of the wavelength λ. For small

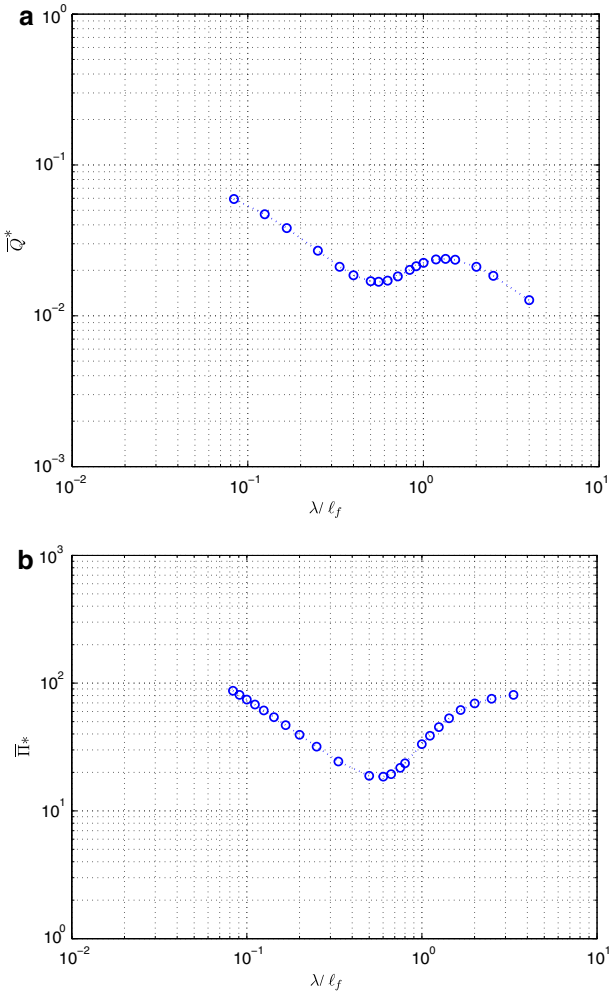

Fig. 8 **a** The time-averaged flow rate as a function of wavelength to film's length ratio; **b** time-averaged power exerted on fluid by the film as a function of wavelength to film's length ratio

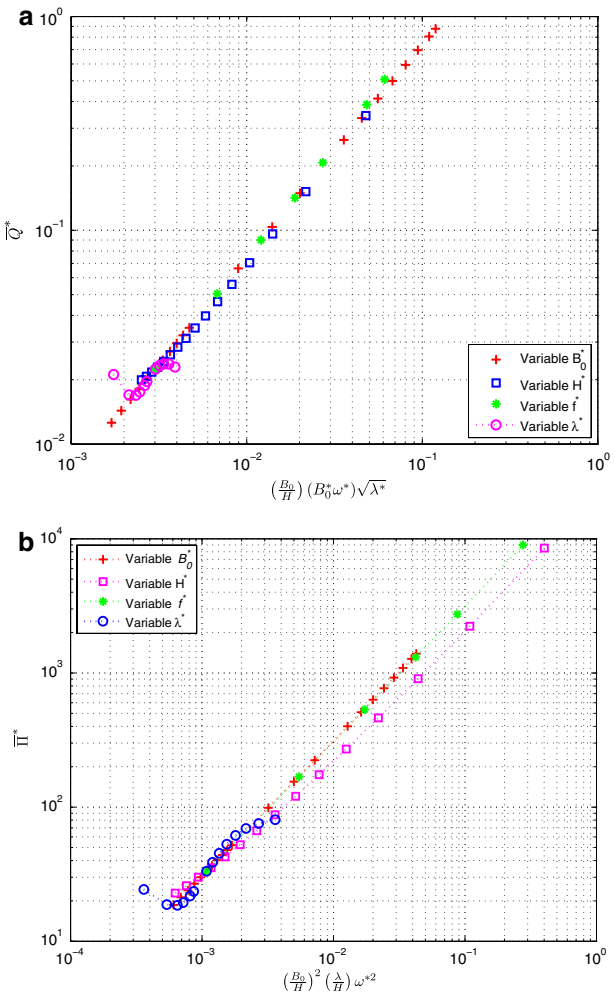

Fig. 9 **a** Combined effects of amplitude, frequency, wavelength and channel height on time-averaged flow rate versus the flow rate parameter; **b** combined effects of amplitude, frequency, wavelength and channel height on time averaged power exerted on fluid versus the power parameter

wavelengths, $\lambda \leq \ell_f/2$, nondimensional power exerted on fluid by the film decreases linearly with respect to the wavelength according to (21). But for $\lambda \geq \ell_f/2 = H$, a different pattern emerges and the power linearly increases with the wavelength. According to the analysis carried out by (Katz 1974), when the wavelength is comparable to the separation between the channel walls, leading order of the average rate of work is given by

$$\bar{\Pi}_{\infty,\lambda\sim H} \sim \mu c^2 k B^2 = \mu\omega^2 B^2 \lambda. \tag{22}$$

For that regime, the pressure itself varies proportional to the wavelength. For very large wavelengths compared to the film's length, uniform steady flow can not be maintained since the motion of the finite film turns into a simple uniform vertical motion of a parabolic curve given by (11) (see Fig. 1), and the propagation of waves diminishes. This behavior manifests itself as leveling off of the curve for large wavelengths in Fig. 8b.

In Fig. 9a, combined effects of amplitude, frequency, wavelength and channel height are put together to characterize the flow rate. From what are depicted in Figs. 6a, 7a and 8a, a flow rate parameter is defined as follows,

$$C_Q = \left(\frac{B_0}{H}\right)\left(B_0^*\omega^*\right)\sqrt{\lambda^*}. \tag{23}$$

Dimensionless average flow rate which is based on the scales provided in Tables 1 and 2 scales with the flow rate parameter, C_Q, given in (23). As the wavelength dictates the flow regime of the finite-length film, only a portion of the wavelength simulations match to this general behavior for wavelengths comparable to the base case, which is used in parametric simulations for amplitude, frequency and the channel height.

In Fig. 9b, time-averaged power exerted on the fluid is plotted against a power parameter that puts together the parametric behavior of nondimensional power, which is shown in Figs. 6b, 7b and 8b, as given by,

$$C_{\Pi} = \left(\frac{B_0}{H}\right)^2 \left(\frac{\lambda}{H}\right) \omega^{*2}. \tag{24}$$

All four curves coincide except for the parametric wavelength curve, which follows the trend only partially, as also observed in Fig. 9b and discussed above.

The power coefficient given by (24), in effect, is derived for constant viscosity. Based on (14) and (15) it is clear that the power exerted on the fluid must scale with the viscosity of the fluid linearly. In fact, an alternate and common nondimensionalization of the pressure and shear stress is based on the scale, $\mu U_0/\ell_0$. If the viscosity were used in nondimensionalization of stress variables and the power, then, without loss of generality (24) would have been used directly without including the effect of viscosity additionally in practical calculations.

4 Conclusion

A dynamic pump, which uses the propulsion mechanism of microorganisms such as spermatozoa, is demonstrated and analyzed by means of numerical simulations. The mechanism, which relies on the effectiveness of traveling-wave deformations on an elastic-thin film immersed in the fluid inside a channel, is a viable option for the actuation of micropumps and propulsion of autonomous microrobots. The steady-periodic flow due to traveling-wave deformations on the film is modeled with Stokes equations and solved on a deforming mesh with the ALE method using commercial software, COMSOL.

Use of a finite-length film results in two different flow regimes as the wavelength varies: (1) for small wavelengths, $\lambda \ll \ell_f$, variations in the pressure and the velocity away from the film are small compared to the mean flow, which sustains an almost-steady rate through the channel; (2) for wavelengths comparable to the length of the film, $\lambda \sim \ell_f$, the pressure and the velocity vary throughout the channel as the deformation-wave propagates on the film resulting in large circulations in the channel and an oscillatory flow.

Parametric dependence of the flow rate and the rate-of-work done on the fluid by the film with respect to the ratio of the deformation amplitude to the channel height, frequency and wavelength is obtained by means of a number of numerical simulations. The relative effect of the amplitude-to-channel-height ratio and the frequency (wave speed for constant wavelength) is found to be in accordance with the former asymptotic analytical results for the infinite-film qualitatively. Independent effects of the amplitude, channel height, frequency and partially the wavelength are grouped into two parameters, one for the flow rate, $C_Q = (B_0/H)\left(B_0^*\omega^*\right)\sqrt{\lambda^*}$, and one for the rate-of-work, $C_\Pi = (B_0/H)^2\,(\lambda/H)\omega^{*2}$.

References

Batchelor GK (2000) An introduction to fluid dynamics. Cambridge Mathematical Library, Cambridge University Press, USA

Bourouina T, Bosseboeuf A, Grandchamp J-P (1997) Design and simulation of an electrostatic micropump for drug-delivery applications. J Micromech Microeng 7:186–188

Brennen C, Winet H (1977) Fluid mechanics of propulsion by cilia and flagella. Ann Rev Fluid Mech 9:339–398

Bruschi P, Diligenti A, Piotto M (2002) Micromachined gas flow regulator for ion propulsion systems. IEEE Trans Aerosp Electron Syst 38:982–988

Childress S (1981) Mechanics of swimming and flying. Cambridge Studies in Mathematical Biology, Cambridge University Press, New York

COMSOL AB (2007) Comsol Multiphysics Modelling Guide

Duarte F, Gormaz R, Natesan S (2004) Arbitrary Lagrangian–Eulerian method for Navier–Stokes equations with moving boundaries. Comput Meth Appl Mech Eng 193:4819–4836

Dutta P, Beskok A (2001) Analytic solution of combined electroosmotic/pressure driven flows in two-dimensional straight channels: finite Debye layer effects. Anal Chem 73(9):1979–1986

Feng G-H, Kim ES (2005) Piezoelectrically actuated dome-shaped diaphragm micropump. J Microelectromechan Syst 14(2):192–199

Gardeniers JGE, van den Berg A (2004) Lab-on-a-chip systems for biomedical and environmental monitoring. Anal Bioanal Chem 378:1700–1703

Gray J, Hancock GJ (1955) Propulsion of sea-urchin Spermatozoa. J Exp Biol 32:802–814

Homsy A, Koster S, Eijkel JCT, Berg A, Lucklum F, Verpoorte E, de Rooij NF (2005) A high current density DC magnetohydrodynamic (MHD) micropump. Lab Chip 5:466–471

Jang J, Lee SS (2000) Theoretical and experimental study of magnetohydrodynamics (MHD) micropump. Sens Actuators A(80):84–89

Katz DF (1974) On the propulsion of micro-organisms near solid boundaries. J Fluid Mech 64(1):33–49

Landau LD, Lifshitz EM (2005) Fluid mechanics. Course of theoretical physics, Elsevier Butterworth-Heinemann, Oxford

Laser DJ, Santiago JG (2004) A review of micropumps. J Micromech Microeng 14:R35-R64

Lemoff AV, Lee AP, Miles RR, McConaghy CF (1999) An AC magnetohydrodynamic micropump: towards a true integrated microfluidic system. Transducers' 99 10th international conference on solid-state sensors and actuators, Sendai Japan, 7–10 June

Li HQ, Roberts DC, Steyn LJ, Turner KT, Carretero JA, Yaglioglu O, Su Y-H, Saggere L, Hagood NW, Spearing SM, Schmidt MA, Mlcak R, Breuer KS (2000) A high frequency high flow rate piezoelectrically driven MEMS micropump. In: Proceedings IEEE solid state sensors and actuators workshop hilton head

Lowe CP (2003) Dynamics of filaments: modeling the dynamics of driven microfilaments. Phil Trans R Soc Lond B(358):1543–1550

Meyns B, Sergeant P, Nishida T, Perek B, Zietkiewicz M, Flameng W (2000) Micropumps to support the heart during CABG. Eur J Cardiothorac Surg 17:169–174

Munson BR, Young DF, and Okiishi TH (2006) Fundamentals of fluid mechanics. Wiley, New York

Piefort V (2001) Finite element modelling of piezoelectric active structures. Ph.D. thesis submitted to faculty of applied sciences. Ph.D. Thesis, Université Libre De Bruxelles

Piefort V, Henrioulle K (2000) Modelling of smart structures with colocated piezoelectric actuator/sensor Pairs: influence of the in-plane components. Identification, control and optimization of engineering structures. Civil-Comp Press, Edinburgh

Polla DL, Erdman AG, Robbins WP, Markus DT, Diaz-Diaz J, Rizq R, Nam Y, Bricker HT, Wang A, Krulevitch P (2000) Microdevices in medicine. Annu Rev Biomed Eng 2:551–576

Polson NA, Hayes MA (2000) Electroosmotic flow control of fluids on a capillary electrophoresis microdevice using an applied external voltage. Anal Chem 72(10):1088–1092

Purcell EM (1977) Life at Low Reynolds number. Am J Phys 45(1):3–11

Sir Taylor G (1951) Analysis of the swimming of microscopic organisms. Proc Roy Soc A(209): 447–461

Tabak AF (2007) Simulation based experiments of traveling-plane-wave-actuator micropumps and microswimmers. MS Thesis, Sabanci University (in preparation)

Tabak AF, Yeşilyurt S (2007) Numerical simulations and analysis of a micropump actuated by travelling plane waves. SPIE symposium on MOEMS-MEMS 2007 Micro and Nanofabrication, San Jose, CA

Van Lintel HTG,Van de Pol FCM, Bouwstra S (1988) A piezoelectric micropump based on micromachining of silicon. Sens Actuators 15:153–167

Wang CH, Lee GB (2005) Automatic bio-sensing diagnostic chips integrated with micro-pumps and micro-valves for multiple disease detection. Biosens Bioelectron 21:419–425

Winslow A (1967) Numerical solution of the quisilinear Poisson equations in a nonuniform triangle mesh. J Comp Phys 2:149–172

Zengerle R, Kluge S, Richter M, Richter A (1995) A bidirectional silicon micropump. In: Proceedings of IEEE micro electro mechanical systems MEMS'95

Zhang Y, Dunn ML (2002) Vertical electrostatic actuator with extended digital range via tailored topology. In: Proceedings of SPIE, 4700, p 147

Zhang T, Wang Q-M (2006) Performance evaluation of a valveless micropump driven by a ring-type piezoelectric actuator. IEEE Trans Ultrason Ferroelectr Freq Control 53(2):463–473

Zhang L, Koo J-M, Jiang L, Asheghi M, Goodson KE, Santiago JG, Kenny TW (2002) Measurements and modeling of two-phase flow in microchannels with nearly constant heat flux boundary conditions. J Microelectromech Syst 11(1):12–19